
A NOVEL PATCH-BASED TDA APPROACH FOR COMPUTED TOMOGRAPHY

Dashti A. Ali^a, Aras T. Asaad^d, Jacob J. Peoples^b, Mohammad Hamghalam^a, Alex Robins^c, Mane Piliposyan^a, Richard K. G. Do^b, Natalie Gangai^b, Yun S. Chun^f, Ahmad Bashir Barezai^c, Jayasree Chakraborty^b, Hala Khasawneh^b, Camila Vilela^b, Natally Horvat^b, João Miranda^b, Alice C. Wei^c, and Amber L. Simpson^{a,e}

^aSchool of Computing, Queen's University, Kingston, ON, Canada

^bDepartment of Radiology, Memorial Sloan Kettering Cancer Center, New York, USA

^cHepatopancreatobiliary Service, Department of Surgery, Memorial Sloan Kettering Cancer Center, New York, USA

^dMathematical Institute, Oxford University, Oxford, United Kingdom

^eDepartment of Biomedical and Molecular Sciences, Queen's University, Kingston, ON, Canada

^fDepartment of Surgery, University of Texas MD Anderson Cancer Centre, Houston, TX, USA

December 16, 2025

ABSTRACT

The development of machine learning (ML) models based on computed tomography (CT) imaging modality has been a major focus of recent research in the medical imaging domain. Incorporating robust feature engineering approach can highly improve the performance of these models. Topological data analysis (TDA), a recent development based on the mathematical field of algebraic topology, mainly focuses on the data from a topological perspective, extracting deeper insight and higher dimensional structures from the data. Persistent homology (PH), a fundamental tool in the area of TDA, can extract topological features such as connected components, cycles and voids from the data. A popular approach to construct PH from 3D CT images is to utilize the 3D cubical complex filtration, a method adapted for grid-structured data. However, this approach may not always yield the best performance and can suffer from computational complexity with higher resolution CT images. This study introduces a novel patch-based PH construction approach tailored for volumetric medical imaging data, in particular CT modality. A wide range of experiments has been conducted on several datasets of 3D CT images to comprehensively analyze the performance of the proposed method with various parameters and benchmark it against the 3D cubical complex algorithm. Our results highlight the dominance of the patch-based TDA approach in terms of both classification performance and time-efficiency. The proposed approach outperformed the cubical complex method, achieving average improvement of 10.38%, 6.94%, 2.06%, 11.58%, and 8.51% in accuracy, AUC, sensitivity, specificity, and F1 score, respectively, across all datasets. Finally, we provide a convenient python package, Patch-TDA, to facilitate the utilization of the proposed approach.

Keywords Topological data analysis, Persistent homology, Medical imaging, Computed tomography, Machine learning, 3D Cubical complex

1 Introduction

The development of computer aided diagnostic tools has gained significant interest in recent years, particularly in the prognostication of cancer where they offer the potential to derive non-invasive biomarkers from various medical imaging technologies. Computed tomography (CT) scans are, in particular, a primary source of data to build robust machine learning (ML) models since they provide rich insights about the disease through their volumetric nature. Leveraging this comprehensive imaging modality, many ML algorithms have been proposed across the last decade, and new ones continue to appear with alarming frequency. Classical ML approaches such as radiomics or sophisticated deep

learning-based approaches have shown success in numerous tasks. However, radiomic features, which rely on pixel-wise comparisons, are often sensitive to variations in image acquisition settings, for instance differences in resolution or contrast [1, 2, 3], and deep learning methods, while addressing some of these challenges, are criticized for insufficient explainability, due to opaque decision-making, and their high computational demands hinder their accessibility [4, 5, 6]. Topological data analysis (TDA) has emerged as a promising approach, to address some of these limitations, providing a unique way to extract richer patterns and insight from data. TDA is built mainly upon theoretical concepts from a field of mathematics called algebraic topology, analyzing the topological structure of the data across different scales, revealing complex relationships and uncovering hidden patterns that may not be visible to the naked eye [7, 8].

When it comes to developing ML models on medical imaging data with volumetric structure (e.g., 3D CT scans), employing robust feature engineering approaches is vital, particularly one that take advantage of the temporal information presents in the data. A popular choice in the realm of TDA to extract topological features by constructing persistent homology (PH) from such data is 3D cubical complex filtration [9, 10]. Although this approach has shown success on grid structured data, such as 2D images, it may not provide the optimal result and be time-efficient on high resolution volumetric data. In this study, we propose a patch-based PH construction method to address these challenges. This approach mainly concentrates on the transformation of the volumetric data, with specific focus on 3D CT scans modalities in this study, to an d -dimensional point cloud through the process of 3D image patch summarization to d -dimensional point. With a point cloud representing the 3D image, we have utilized alpha complex filtration, an efficient approach to construct PH from point cloud data. Note that another advantage of this approach is that, unlike cubical complex, with point cloud data higher dimensional structures beyond connected components, loops and enclosed voids can be explored. In our previous work [11], a PCA-based approach was proposed which only utilized PCA for patch intensities summarization. However, this study provides a more comprehensive technique that employs different patch intensities summarization approaches and also integrates compressed patch coordinates representation into the pipeline outperforming the previous approach.

TDA has demonstrated significant success in the development of models based on different medical imaging modalities such as X-ray, CT, MRI, and ultrasound [12]. For instance, in the assessment of tumour heterogeneity in lung adenocarcinomas based on CT images [13], analysis of osteoarthritis from MRI images [14], classification of chronic obstructive pulmonary disease and explaining the geometric structure of the airway system through lung CT images [15], evaluation of the accuracy of hepatic cancer prediction via MRI images [16], distinguishing squamous cell carcinoma from adenocarcinoma and benign from malignant tumours in lung CT images [17], unveiling the dynamical organization of the brain using fMRI data [18] and characterization of the 3D structure of trabecular bone and predicting bone strength using bone MR images [19]. To the best of our knowledge, the proposed technique is one of the first alternative approaches to cubical complex-based PH computation for volumetric medical imaging data.

The first contribution of this paper is the proposal of a patch-based PH construction approach for 3D CT imaging data that strive to achieve both better classification performance and efficiency than the classical cubical complex filtration approach. The second contribution of this work concerns with a comprehensive analysis of different patch-to-point-cloud transformation techniques to be employed in the process of transforming volumetric data to point cloud. This includes an extensive set of experiments on four distinct CT datasets involving clinically relevant and challenging classification tasks, such as predicting patient response to therapy. The third contribution of this study involves a systematic benchmarking of the proposed patch-based PH construction approach, on four datasets of CT scans, against the classical 3D cubical complex filtration method in terms of classification performance and time efficiency. Finally, the implementation of the proposed patch-based TDA algorithm is encoded into a convenient python package to facilitate user experimentation with the approach.

2 Methods

2.1 Topological Data Analysis

Topology is a field of mathematics concerned with the connectivity and continuity properties of objects. An important aspect of the topological spaces and their properties is their ability to be coordinate free, invariant under continuous deformation and to be expressed in compressed form [8]. Using tools in the field of TDA we can extract topological invariants of complex and high dimensional data which are stable in terms of small perturbations to input noise and can be employed with various ML tasks such as classification. Topological invariant examples studied in this work are connected components, loops and cavities (i.e. enclosed voids).

These topological invariants can be quantified by what are called Betti numbers. The first N Betti numbers are used to differentiate objects with differing topology in N -dimensional space. For instance, the Betti number of 2D objects includes (β_0, β_1) , and $(\beta_0, \beta_1, \beta_2)$ for 3D, where β_0 , β_1 and β_2 refer to connected components, loops and voids respectively. Although this characterization is simple to describe in abstraction, its practical computation requires a

smart machinery. This can be achieved through homology theory, a well-established technique in algebraic topology. To apply homology theory to compute Betti numbers of objects, they must be represented in combinatorial structures such as simplicial or cubical complexes [20].

PH is a principal tool in the field of TDA, used to quantify the shape of data at different scales (computing Betti numbers), tracking the evolution of topological features such as connected components, cycles and cavities. Homology provides the theoretical framework for persistent homology. In order to compute topological features from data, one need to utilize a combinatorial approach, known as filtration, such as a simplicial or cubical complex, to build PH. A simplicial complex (SC) is a topological space build from a set of multi-dimensional triangular subsets of \mathbb{R}^n , by joining some of them together along their boundary components such as nodes, edges and faces. SCs transform the continuous domain of topological spaces to the discrete domain of data [21]. Figure 1 demonstrate this process on a sample point cloud data. The evolution of topological structures, including connected components and loops can be observed from the figure as the filtration process advances from left to right, by increasing the distance threshold. Through this process, each topological feature is tracked using a horizontal bar, where the start of the bar indicates when the feature first appears, and the end of the bar indicates when the feature disappears or merges with another feature. A collection of such bars is called a persistence barcode (PB). The concept of PBs will be explained further in later sections. In general, the process of acquiring topological features from data involves two main steps. First constructing PH from the data through a filtration method, to obtain PBs and second, featurizing the space of PBs using vectorization methods to be ready for ML algorithms or for further analysis. In this work, we utilize two distinct filtration approaches: alpha complex, for building PH from point cloud data, and the cubical complex which is tailored for grid-structured data such as digital images. In the following sections, these methods will be explained in detail.

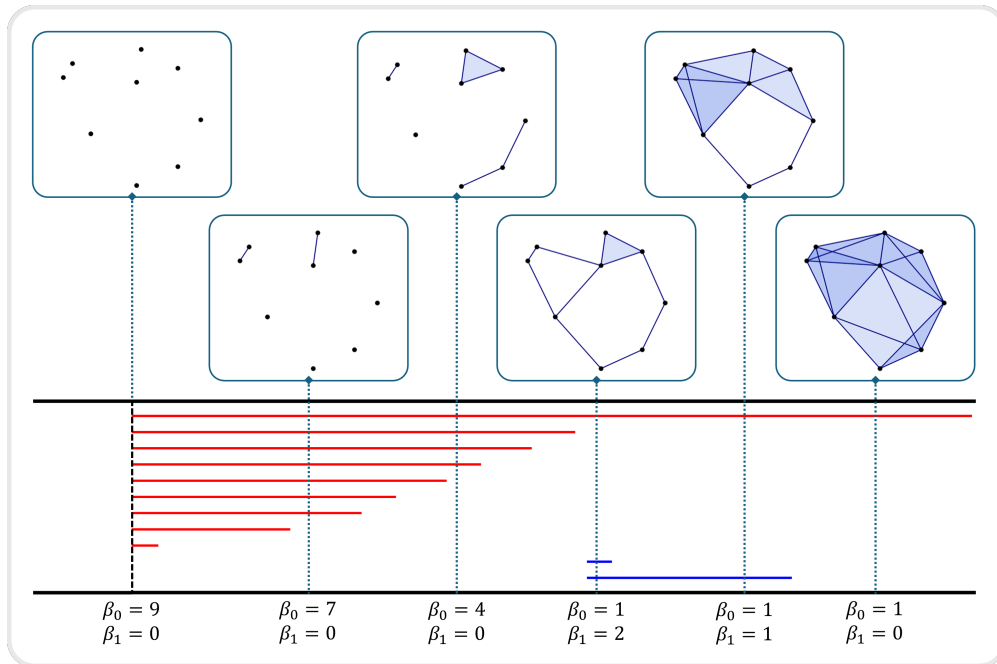


Figure 1: Generating persistent barcodes from a sample point cloud. In the far left side, at the beginning, the distance threshold is zero, hence each point is an independent component (nine red bars start at zero correspond to nine points). Each red bar tracks the evolution of a homological feature in dimension zero (connected components). As we move to the right, the threshold is increased and points, whose distance are within the threshold, will connect (merge into one component). Eventually, all the points are merged into a single connected component. During this process, loop structures, homological feature in dimension one, are also forming and eventually vanishing as the threshold is increased (indicated by blue bars). The start and end of a bar indicate the birth and death of a feature, respectively, and the longer the bar, the more persistent the feature is. The collection of the red bars is referred to as PBs in dimension zero, while the blue bars forms PBs in dimension one.

2.2 Alpha Complex

In the context of PH, alpha complex provides a computationally efficient approach to build multi-resolution topological features of a set of n -dimensional points. Alpha complex is a family of sub-complexes from the Delaunay triangulations of a point set and provides a geometrically meaningful approximation of the union of balls centred at the input points. As the parameter ε increases, the radius of these balls grows, and new simplices are added to the complex in a manner that respects the geometry of the data. Next, we describe alpha complex mathematically together with necessary definitions.

Definition 2.1 (Cover). Let $X = \bigcup_{i \in I} U_i$ be a topological space. Then, the cover of X is defined as a non-empty and finite collection of open sets $\mathcal{U} = \{U_i\}_{i \in I}$. More specifically, \mathcal{U} is called a *good cover* if all individual sets $U_i \in \mathcal{U}$ and all finite, non-empty intersections of those sets are contractible, i.e., they can be continuously deformed into a single point [22, 23].

Definition 2.2 (Nerve). The nerve \mathcal{N} of \mathcal{U} can be defined by the following criteria:

1. $\phi \in \mathcal{N}$.
2. If $\bigcap_{j \in J} U_j \neq \phi$ for $J \subseteq I$, then $J \in \mathcal{N}$.

Definition 2.3 (Voronoi cell). Let X be a finite set of points in \mathbb{R}^d . The Voronoi cell of a point x in X is the set of points $V_x \subseteq \mathbb{R}^d$ for which x is the closest point in X , i.e. $V_x = \{u \in \mathbb{R}^d : |u - x| \leq |u - x'|, \forall x' \in X\}$.

Definition 2.4 (Delaunay complex). The Delaunay complex of a finite set $X \in \mathbb{R}^d$ is the nerve of the corresponding Voronoi diagram.

The intersection of the Voronoi cell V_x with $B(X, \varepsilon)$ is defined as $\mathbb{R}_\varepsilon(x)$, i.e., $\mathbb{R}_\varepsilon(x) = V_x \cap B(X, \varepsilon)$ for every $x \in X$. With these definitions in place, we can now formally define alpha complex.

Definition 2.5 (Alpha complex). The alpha complex $\mathcal{A}_\varepsilon(X)$ is the nerve of the covers shaped by $\mathbb{R}_\varepsilon(x)$ for all $x \in X$, [24] i.e.

$$\mathcal{A}_\varepsilon(X) := \{\sigma \in X \mid \bigcap_{x \in \sigma} \mathbb{R}_\varepsilon(x) \neq \phi\}.$$

2.3 Cubical Complex

Cubical complex is a combinatorial approach to construct PH from grid-structured data, for example, 2D or 3D digital images. Cubical complex is constructed by ordering the cells (vertices, edges, squares, etc.) using a scalar function, voxel intensity value in the context of 3D CT scan images where cells are added to the complex based on the ascending order of their voxel intensity values. Mathematically, a finite cubical complex in \mathbb{R}^3 is a collection of cubes aligned on the grid G^3 , satisfying some conditions analogous to a SC [25]. A 3-dimensional image can be represented as a map $\eta : I \subseteq G^3 \rightarrow \mathbb{R}$. For an element $v \in I$, called a voxel (pixel when $d = 2$), its intensity or grayscale value is given by $\eta(v)$. There are several ways to represent digital images as cubical complexes. A common construction is to represent each voxel as a top-dimensional 3-cube and include all of its faces in the complex. A 3D CT scan comes with a natural filtration within the grayscale values of its voxels. A function is obtained on the resulting cubical complex C as follows by extending the values of voxels to all the cubes $\omega \in C$:

$$\eta'(\omega) := \min_{\omega \text{ face of } \tau} \eta(\tau).$$

Given the cubical complex C constructed from I and let

$$C_i := \{\omega \in C \mid \eta'(\omega) \leq i\},$$

be the i -th sublevel set of C . This yields a filtration of the cubical complex defined as $\{C_i\}_{i \in \text{Im}(I)}$ and indexed by the values of the function η . [25].

Since visualizing this filtration process on a 3D image is challenging on paper, for simplicity, this process is illustrated on a 4x4 patch of a grayscale image in Figure 2. Pixels with higher intensity are filtered and added to the complex as the filtration value is increased. Concurrently, the construction of PBs is appeared in the same figure, below the grid filtration process. The appearance (birth) and vanishing (death) of connected components and loops are highlighted by H_0 and H_1 respectively. In addition to these structures, the birth and death of cavities (voids), denoted by H_2 , can also be computed when this procedure is applied on 3D CT images.

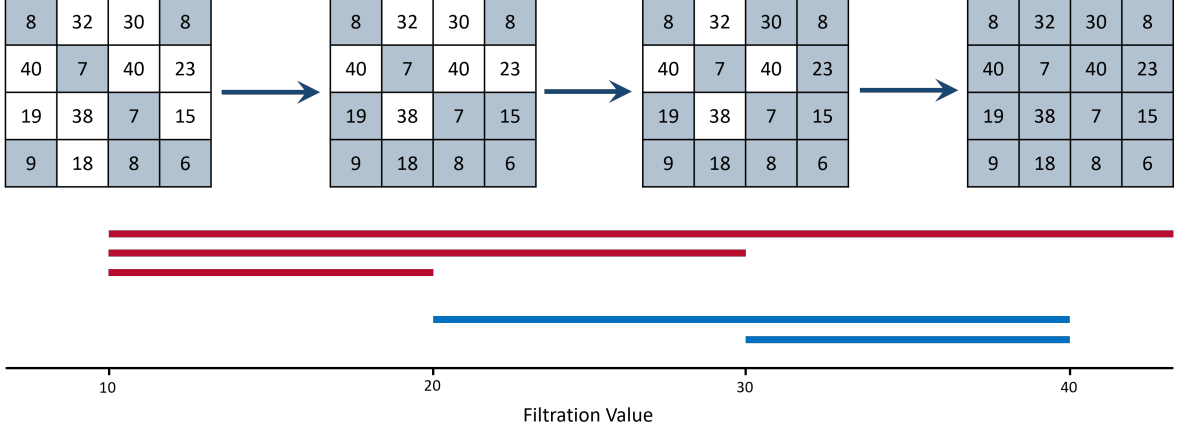


Figure 2: Cubical complex filtration and PBs representations in dimension zero and one for a 4x4 grayscale image patch. The red bars highlight the life line of the connected pixels, while the blue bars correspond to the loops appear between the connected pixels.

2.4 Persistence Barcodes

A persistence barcode can be expressed as

$$B = [(p_1, q_1), (p_2, q_2), \dots, (p_n, q_n)],$$

where $B(p, q)$ corresponds to a bar with birth at p and death at q . Note that a barcode has a multiset structure, meaning that an element (p, q) in the barcode B may occur multiple times [26]. Therefore, the barcode B has a multiplicity function $\mu : B \rightarrow \mathbb{Z}_{>0}$.

Here we demonstrate the cubical complex filtration on a sample 2D image of a pancreatic tumour ROI due to the limitation of visualizing the 3D cubical complex filtration on the 3D tumour ROI. A summary of this procedure is illustrated in Figure 3. The process utilizes an ordered list of distinct pixel intensity values within the image as the filtration parameter. Taking one value from the list at a time and filling in those pixels in the image whose intensity values are less than or equal to the current threshold value, connected components starts to appear, it can be either a single filled in pixel or pixels that are connected to each other. Following this filtration process and by increasing filtration thresholds, some of these connected pixels may join others quickly while some may persist to stay independent for longer. For example, neighbouring pixels with less varying intensities will join each other quickly while a pixel or a group of adjacent pixels whose intensity values stands out from the surrounding ones will stay as a single connected component for longer time. This cluster of pixels could be a darker spot in the tumour ROI revealing specific pathological patterns. Fortunately, we can keep track of all these short and long living connected components using persistent homology barcodes by representing the lifeline of each structure as a bar with its starting point (birth) to be the threshold where it starts to appear and the end point (death) indicating the threshold where it joins another cluster, and hence a collection of such bars forms a barcode. Other structures, beyond the connected pixels, whose evolution can be tracked during the filtration process are the loops. A loop structure could be a single or a group of trapped non-filled pixels surrounded by connected pixels whose values are less than the filtration threshold. This could be a lighter spot in the image or a larger region indicating separation of tumour (or soon to be a tumour) with respect to its surrounding. Utilizing this filtration process, both local and global topological features present in the image can be captured. Note that, when the filtration process is applied to the 3D tumour ROI, instead of the 2D slice only, beside the connected components and cycles, the evolution of enclosed voids, another higher dimensional structure, can also be tracked to generate the corresponding void-representing barcode.

2.5 Vectorization

The PBs acquired via a filtration process (here alpha or cubical complex), are not directly compatible with ML algorithms since they are not easily amenable to statistical analysis; for instance, their Fréchet mean is not unique [26]. To overcome this bottleneck, barcodes are often embedded into vector spaces (e.g., Hilbert or Banach spaces), where well-defined inner products enable standard ML operations. Several vectorization techniques have been proposed in recent years to transform PBs into suitable feature vectors [27, 28, 29, 30]. Persistent statistical vectorization is a frequently used approach to featurize the space of PBs which provides a compact summary of PBs and has shown

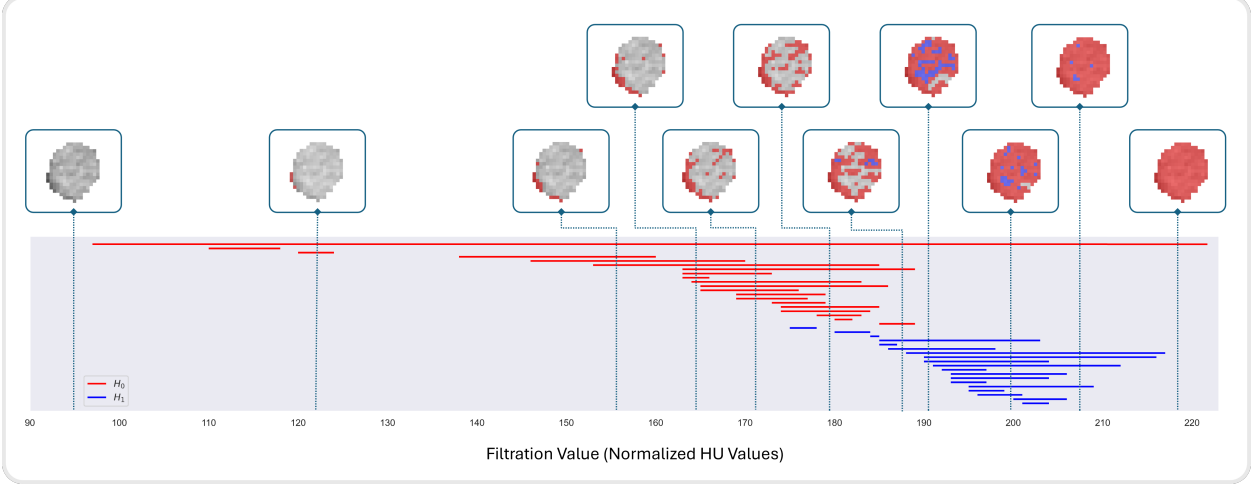


Figure 3: A summary illustration of the process of cubical complex filtration on a sample 2D image, the ROI of a slice of a pancreatic tumour. For visualization purpose, we used the normalized HU values in this example. As the filtration value increases, the structure of connected pixels changes, and loop structures surrounded by the connected pixels appear and eventually vanish. The life timeline of connected components and loops are highlighted with the red and blue bars respectively.

robustness and success in comparison with other vectorization approaches to analysis digital images [31]. This approach constructs a feature vector by computing different statistical quantities from a given PB including the mean, median, standard deviation, full range, inter-quartile range, and the 10th, 25th, 75th, and 90th percentiles of the birth p , the death q , the lifespans $q - p$ and the midpoints of the bar intervals $[p, q]$ in a PB. Entropy and bar counts are also included to further extend the feature set. The entropy of μ , introduced in [30], is a real number defined as follows:

$$E_\mu := - \sum_{[p,q] \in B} \mu_{p,q} \cdot \left(\frac{q-p}{L_\mu} \right) \cdot \log \left(\frac{q-p}{L_\mu} \right),$$

where L_μ denotes the weighted sum

$$L_\mu := \sum_{[p,q] \in B} \mu_{p,q} \cdot (q - p).$$

2.6 Patch-based TDA: The Proposed Approach

At its core, patch-based TDA is an approach to constructing PH from volumetric data (e.g., 3D CT images), primarily focusing on transforming the data into a point cloud structure from which various topological features such as connected components, loops, and voids can be extracted. The intuition behind this technique is to reduce the effect of noisy voxels, present in 3D medical images, through image patch summarization while keeping important information from the patch including the location of the patch in the image and its voxel intensity values statistical summary. This process starts by taking cubic patches of size $n \times n \times n$ voxels from the input 3D image. selecting a cubic patch of, for instance $3 \times 3 \times 3$ voxels, from a 3D image, then flattening and extending it with its approximate central voxel coordinates will result in a vector containing 30 values. A straight forward approach would be to consider this vector as a point in 30 dimensions. However, this approach may not be ideal since this vector may contain values from the noisy voxels and building PH for a CT scan of large sizes is a tedious task and requires extensive computational resources. Furthermore, the dimension of the resulting flattened patch will increase cubically as the patch size grows. To overcome this issue, we propose a novel patch-to-point conversion method serving as the backbone of the patch-based TDA approach to transform 3D images to point clouds. This patch-to-point conversion mechanism encompasses two sub-tasks: one to convert the patch coordinates to a compact representation, called coordinates encoding, and the second sub-task, called intensity encoding, to summarize the values of the flattened patch into a smaller vector.

For the coordinate encoding part, after preliminary experiments with a number of methods such as Morton code (Z -order curve) and L_2 norm, the Morton code algorithms [32] is utilized to compress the three coordinates (x , y and z), corresponding to the approximate centre of the patch, to a single value. In parallel, for the second part of the pipeline, intensities encoding, two distinct approaches are considered: 1) employing PCA to reduce the dimension of

the flattened patch and consequently utilizing d PCA components to create the point cloud, 2) computing statistical quantities (stats), for instance mean, mode and median, from the flattened patch to create the final point where each one of these stats corresponds to an axis in the space. This procedure is demonstrated in Figure 4, part A. Finally, applying the patch-to-point transformation techniques on all the patches taken from a volumetric ROI of a 3D image, a point cloud is obtained as depicted in Figure 4, part B. It is worth mentioning that, during this process only cubic patches with at least one voxel corresponding to the ROI are considered and converted to points contributing to the final point cloud, i.e, void or empty patches are discarded. This step is crucial to enhance the downstream computation of PH from the point cloud.

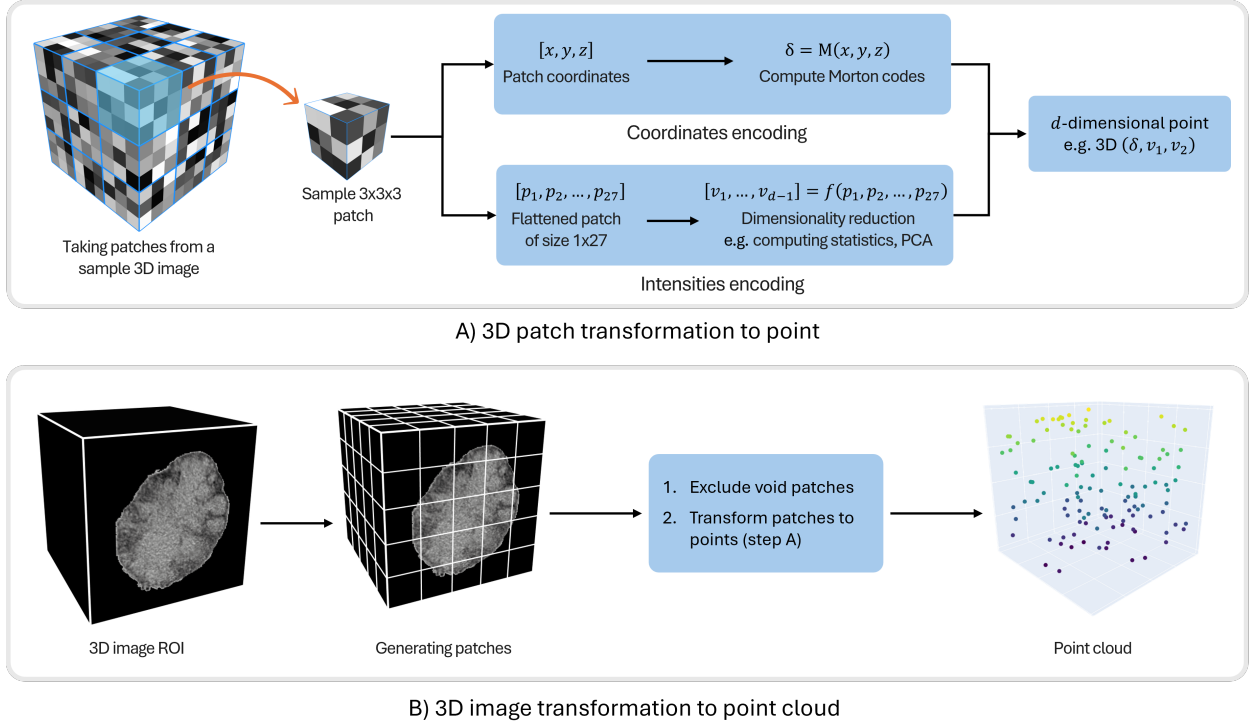


Figure 4: The process of generating a d -dimensional point from a 3D patch of $3 \times 3 \times 3$ voxels from a 3D image is demonstrated in part A, and the transformation of a 3D image ROI into a 3D point cloud is visualized in part B.

There are different ways to compute PH from a point cloud. In this study, alpha complex filtration [33, 34] is utilized to compute PH in dimensions zero, one and two, corresponding to the number of connected components, loops, and cavities, respectively. Hence, obtaining three persistence barcodes. This follows by the vectorization process, computing persistent statistical features for each barcode, yielding three feature vectors. Finally, these feature vectors are concatenated and used as input to a ML classifier. This workflow is illustrated in Figure 5.

The first research question in our proposed patch-to-point method concerns determining the optimal patch size. A smaller patch size may include more noisy voxels, whereas a larger one could lead to the loss of important information. In this study, we define the patch size search space as $p = \{3, 4, 5, \dots, 10\}$. The second research question investigates the optimal stats combination to summarize a flattened 3D patch (intensities encoding layer). To address this question, first a stats search space need to be defined to choose the combination from. We set this search space to $s = \{\text{mean, median, mode, standard deviation, interquartile range, entropy, range, minimum, maximum}\}$ which includes some of the most frequently used statistical quantities among others. In what follows, we discuss and show empirically what are the best p and s based on a diverse 3D CT scan datasets described in the next section.

2.7 Datasets

In this work, four diverse datasets of CT scans are utilized in order to conduct a comprehensive assessment of the patch-based TDA approach and benchmark its performance. These include the publicly available dataset of kidney tumours KiTS19 [35], the FLARE22 dataset from MICCAI FLARE22 challenge [36, 37] which is a collection of

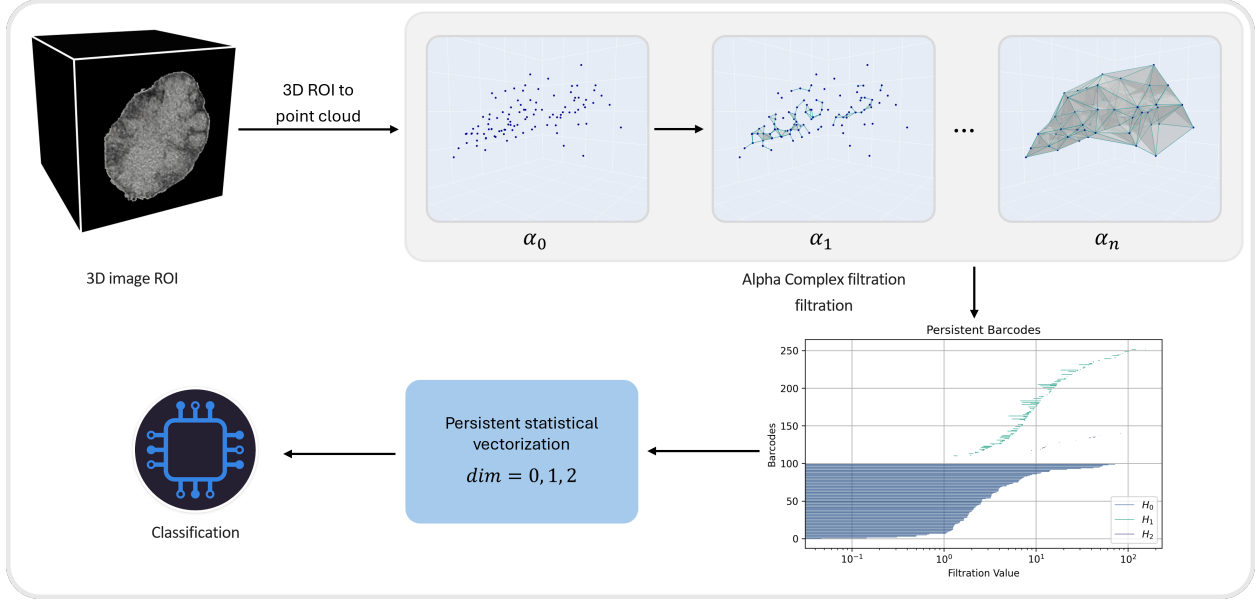


Figure 5: Patch-based TDA pipeline.

abdominal CT images, and two in-house datasets. Sample CT slices of different classes of each dataset is illustrated in Figure 6. Table 1 presents a summary of key details about each dataset.

KiTS19: this dataset was obtained from the GitHub repository of the kidney tumour segmentation challenge. It comprises abdominal CT scans and corresponding segmentation masks for 210 patients with kidney tumours. Among them, 70 underwent radical nephrectomy and 140 underwent partial nephrectomy. These surgical procedure types will serve as labels for downstream analysis.

FLARE22: the second dataset, FLARE22, is acquired from the MICCAI FLARE22 challenge. The dataset includes 50 abdominal CT scans alongside the segmentation masks of 13 different abdominal organs: liver, right kidney, spleen, pancreas, aorta, inferior vena cava, right adrenal gland, left adrenal gland, gallbladder, esophagus, stomach, duodenum and left kidney. With 50 CT scans and 13 different ROIs of organs, we obtained a total of 650 ROI images. Although classifying ROI of body organs may not be a clinically relevant task where segmentation masks are already provided, the dataset is solely utilized to design a multi-label classification task and assess the proposed patch-based approach and benchmark it against existing PH-construction methods.

Colorectal liver metastases dataset (CRLM): this dataset includes 590 pre-treatment abdominal CT scans of patients diagnosed with unresectable CRLM and subsequently received chemotherapy at Memorial Sloan Kettering Cancer Centre (MSKCC) comprising 357 cases and MD Anderson Cancer Centre (233 cases). These patients were scanned again eight weeks after the treatment. An in-house developed segmentation model based on 3D U-Net architecture was utilized to obtain the segmentation masks of the tumours [38]. Using pre and post treatment scans patients were categorized based on their response to the therapy using volumetric Response Evaluation Criteria in Solid Tumours (RECIST) [39]. Therefore, patients were grouped as follows: 7 had complete response (CR), 229 had partial response ($PR \geq 65\%$ tumour shrinkage), 48 had progressive disease ($PD \geq 65\%$ tumour growth), and 306 had stable disease (SD, changes between PR and PD). For downstream analysis, CR and PR were grouped as “response” (236 patients), while SD and PD formed the “non-response” group (354 patients).

Pancreas tumours dataset: this final dataset is a collection of pre- and post-treatment abdominal CT scans from 97 patients who underwent neoadjuvant chemotherapy for pancreatic ductal adenocarcinoma (PDAC) at MSKCC. Eight patients were excluded from the analysis due to incomplete or missing pre-treatment scans, or missing RECIST labels. Pancreas tumours were manually segmented from the pre-treatment scans and verified by a board-certified radiologist. Using pre and post treatment scans, RECIST measurements were calculated by a board-certified radiologist. Based on these measurements, patients were grouped according to their response to therapy: 21 cases of progressive disease (PD), 43 cases of stable disease (SD), and 25 cases of partial response (PR). There were no patients with a complete response. Furthermore, PD and SD were grouped into a single class, “non-response”. The final categorization of the dataset includes 25 “response” and 64 “non-response” cases.

Table 1: Summary of Key Details for Each CT Dataset Included in This Study.

Dataset	ROI	Size	Unique Classes & # Samples/Class
KiTS19	Kidney Tumours	210	Partial Nephrectomy (140), Radical Nephrectomy (70)
FLARE22	Abdomen Organs	650	13 Organs (50 each)
Pancreas Tumours	Tumours	89	Responder (236), Non-responder (354)
CRLM	Liver & Tumours	590	Responder (25), Non-responder (64)

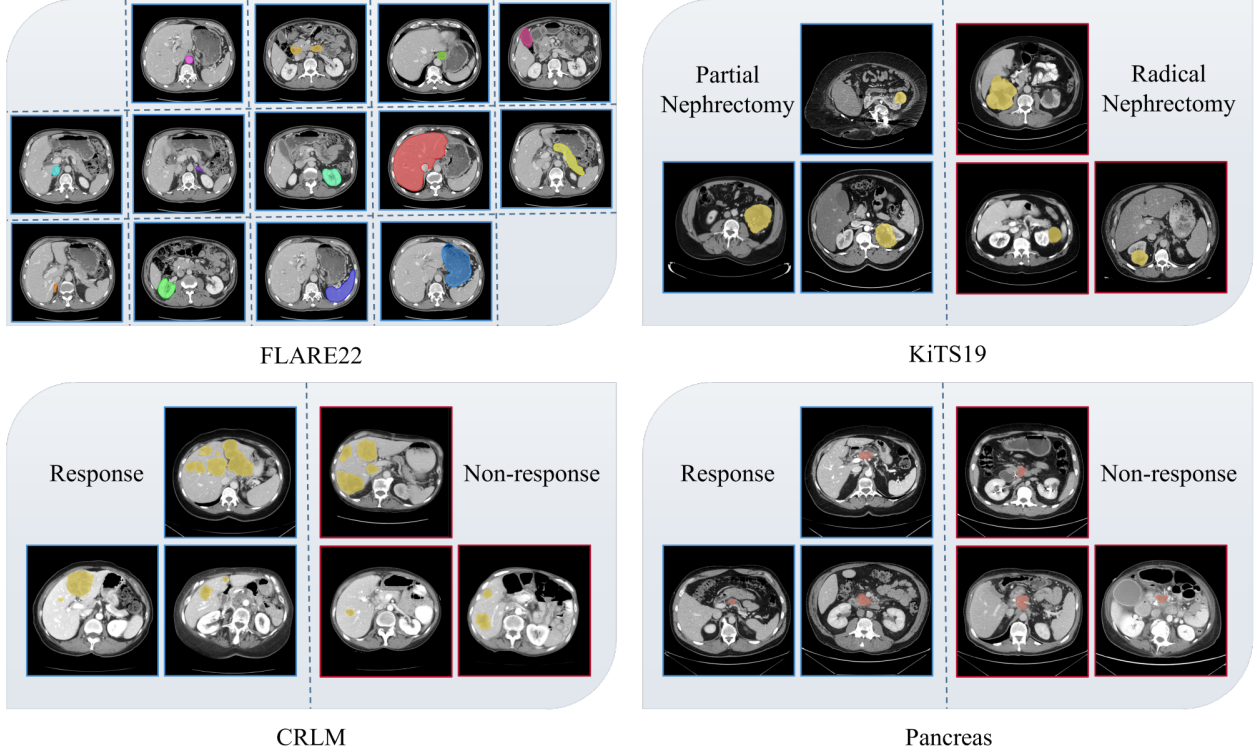


Figure 6: Sample slices of CT images from each dataset are visualized. Sample images of unique classes of each dataset are separated by the dashed lines.

2.8 Experiment Design and Implementation

2.8.1 Data Preprocessing

The first pre-processing phase on each CT dataset was to account for the variable voxel sizes across CT scans; we resampled all CT images to the average spacing within each dataset. The second phase involves applying the corresponding 3D segmentation masks to the CT images, acquired from the previous phase, masking out the targeted region of interest (ROI) and cropping the resulting volume with adequate padding on all sides. For the KiTS19 dataset, the final ROI, which consists of the kidney tumour only, is a 3D volume of $57 \times 220 \times 220$ voxels (i.e., 57 slices of 220×220 voxels each), whereas a 3D window of size $102 \times 290 \times 330$ voxels could accommodate the ROI of each organ in the preprocessed CT images from the FLARE22 dataset. For the CRLM and pancreas tumour datasets, the final ROIs were 3D volumes of $87 \times 323 \times 400$ (including the liver and the tumours) and $33 \times 120 \times 120$ voxels (comprising the tumours only) respectively.

2.8.2 Classification Pipeline Setup

One of the most involved components in the classification pipeline of this study is the feature extraction phase, which includes the transformation of pre-processed ROI volume patches to point clouds, computation of PH in dimensions 0, 1, and 2 using alpha complex filtration, and featurization of PBs via persistent statistical vectorization followed by their concatenation across PH dimensions to obtain a single feature vector. To perform a fair assessment of the features obtained using the patch-based TDA approach, we employed a 5-fold cross-validation strategy for all classification tasks in this work. Stratified 5-fold splitting was used to ensure balanced class distribution across folds. In each fold, the data was standardized using z-score before being passed to a classifier. Five distinct classifiers, Support Vector Machine (SVM), Random Forest (RF), and K-Nearest Neighbors (KNN), Logistic Regression (LR) and Extreme Gradient Boosting (XGBoost) were employed.

2.8.3 Patches and Stats Experiments

The first conducted experiment in this study aimed to find the optimal combinations of patch size and stats. With the predefined search spaces of patch sizes and stats (comprising combinations of two or three stats), we performed a grid search, resulting in 960 experiments. In each trial, a patch size and stats combination were selected from the search spaces, the input 3D ROI volume was transformed into a point cloud and the rest of the classification pipeline was executed. This grid search experiment was consistently applied to each individual dataset. A systematic approach were employed to handle this grid search efficiently and finding the overall best combination of the patch size and stats. In the first stage of the grid search, at each trials, a 5-fold cross-validation (CV) were conducted with SVM, RF, KNN and LR only with a very shallow hyperparameters tuning (with inner CV). In the second stage, only the top 5% of the combinations, with higher average performance across all the classifiers, were selected for the next phase. Finally, we experimented with the selected combinations using all the classifiers (including XGBoost), executing 5-fold CV with deeper hyperparameters tuning.

2.8.4 Patches and PCA Experiments

The second experiment was concerned to identify the optimal patch size when PCA was used to transform patches of the ROI volume into point cloud. A grid search was conducted over the predefined patch size search space while employing PCA as the patch intensities summarization method. We restricted the dimensionality of the points in the point cloud, generated via PCA, to four dimensions (i.e., the Morton value and three PCA components) to ensure a fair comparison with the case where stats were used as patch intensities summarization method. Since, this grid search only contains eight trials (patch size search space), we have utilized similar classification pipeline as in the final stage of the patch-stats grid search experiment.

2.8.5 Benchmarking Experiments

Finally, we benchmarked the patch-based PH construction method against the cubical complex, the classical approach of computing PH for grid-structured data. Two separate experiments were conducted to compare the methods in terms of classification performance and computational efficiency. Considering the volumetric nature of our data, unlike 2D images, the 3D version of cubical complex filtration was employed to construct PH in dimensions zero, one, and two, corresponding to connected voxels, loops, and voids between the voxels respectively. These PBs were then featurized using persistent statistical vectorization and concatenated. The resulting final feature vectors were subsequently passed into the same classification pipeline used in the previous experiments. To benchmark patch-based TDA against the cubical complex in terms of the time required to compute PBs, a sample 3D ROI of the preprocessed CT scans was selected from each dataset, and the average computation time was calculated over 100 trials. This experiment was conducted on a machine equipped with 64 GB of RAM and an Intel Core i7 processor, and there was no resource constraint for the calculations of PH performed by each method. In the next section, the results of all experiments conducted in this study will be reported and discussed.

3 Results

In this study we report relevant evaluation metrics including AUC, accuracy, sensitivity, specificity, and F1 score with standard deviation of each metric across the five folds. The classification results of the grid search experiments on all four datasets are illustrated in Table 2. This includes the results of the grid search for optimal patch size and stats combination and the results of the second grid search for the best patch size with PCA. Results are sorted in terms of overall performance across all metrics and only the best results achieved with each method, stats and PCA, are reported for each dataset. It is apparent from the table that on all datasets, stats obtained better overall results than PCA.

Notably, the PCA results are only marginally below the stats on FLARE22 dataset. It can be seen from the table that both methods of stats and PCA with FLARE22 achieved better results with smaller patch sizes while for the rest of the reported results in the table larger patch sizes (≥ 5) were the winners. In terms of the optimal stats combination, both combinations of two and three stats can be observed in the results however there is no unique combination that would be the optimal choice of stats with all datasets. With regards to the choice of the classifier, LR appears as the clear winner.

The results of benchmarking the patch-based TDA approach against the cubical complex method is depicted in Table 3. Overall, the patch-based approach outperformed the later one on all datasets. It is worth mentioning that the standard deviation of different metrics across the five folds experiments on all datasets is generally lower with the patch-based TDA than with the cubical complex approach which highlights the stability of the first approach.

Finally, we report the benchmarking results of the proposed approach against the cubical complex method in terms of time efficiency. These results are depicted in Table 4, where the average required time to compute PH over 100 trials is calculated for a sample 3D ROI from each dataset. It is apparent from the table that the patch-based TDA approach is significantly more efficient than the cubical complex method across all datasets especially with larger patch sizes which lead to smaller point clouds. For example, on the KiTS19 and pancreas tumours datasets, the proposed method is approximately 128 and 73 times faster than the cubical complex approach respectively. Experimental observations indicate that with the patch-based approach, the PH computation time of 4D point clouds via alpha complex is noticeable slower than its 3D counterpart, which can consequently affect the overall computation time of the proposed approach. Overall, the patch-based TDA approach provides improved results over cubical complex, in terms of both classification performance and time efficiency, particularly with high resolution ROI of CT images.

Table 2: Best Results for Each Dataset with Each Method of Stats and PCA for Patch Summarization.

Dataset	Method	Patch Size	Stats	Model	Accuracy \pm Std.	AUC \pm Std.	Sensitivity \pm Std.	Specificity \pm Std.	FI \pm Std.
KiTS19	Stats	$6 \times 6 \times 6$	mean, median, range	XGBoost	87.14 ± 3.61	90.15 ± 4.75	74.29 ± 3.91	93.57 ± 4.66	79.51 ± 4.89
	PCA	$9 \times 9 \times 9$	-	LR	83.81 ± 4.58	87.5 ± 4.49	82.86 ± 6.39	84.29 ± 7.41	77.52 ± 5.04
FLARE22	Stats	$4 \times 4 \times 4$	mode, entropy	RF	87.54 ± 1.48	99.16 ± 0.2	87.54 ± 1.48	98.96 ± 0.12	87.45 ± 1.43
	PCA	$4 \times 4 \times 4$	-	XGBoost	86.15 ± 2.37	99.15 ± 0.28	86.15 ± 2.37	98.85 ± 0.2	86.11 ± 2.34
Pancreas Tumours	Stats	$6 \times 6 \times 6$	iqr, entropy	LR	75.16 ± 8.97	73.05 ± 9.25	60 ± 20	81.15 ± 10.57	57.22 ± 14.94
	PCA	$10 \times 10 \times 10$	-	LR	69.61 ± 3.65	70.38 ± 9.65	60 ± 31.62	73.33 ± 11.97	49.36 ± 15.56
CRLM	Stats	$5 \times 5 \times 5$	median, entropy, max	LR	60 ± 2.11	63.1 ± 2.71	58.92 ± 7.29	60.74 ± 5.73	53.96 ± 3.33
	PCA	$9 \times 9 \times 9$	-	LR	53.22 ± 7.37	54.13 ± 5.64	54.67 ± 5.61	52.26 ± 9.24	48.47 ± 6.05

Table 3: Benchmarking Patch-Based TDA Against Cubical Complex

Dataset	Method & Parameters	Model	Accuracy \pm Std.	AUC \pm Std.	Sensitivity \pm Std.	Specificity \pm Std.	FI \pm Std.
KiTS19	Cubical Complex	XGBoost	83.33 ± 6.07	87.65 ± 7.43	71.43 ± 20.82	89.29 ± 5.65	72.88 ± 12.32
	Patch-based TDA ($6 \times 6 \times 6$, [mean, median, range])	XGBoost	87.14 ± 3.61	90.15 ± 4.75	74.29 ± 3.91	93.57 ± 4.66	79.51 ± 4.89
FLARE22	Cubical Complex	LR	77.08 ± 2.4	97.49 ± 0.77	77.08 ± 2.4	98.09 ± 0.2	76.89 ± 2.12
	Patch-based TDA ($4 \times 4 \times 4$, [mode, entropy])	RF	87.54 ± 1.48	99.16 ± 0.2	87.54 ± 1.48	98.96 ± 0.12	87.45 ± 1.43
Pancreas Tumours	Cubical Complex	LR	55.03 ± 11.84	58.44 ± 9.85	68 ± 17.89	49.87 ± 18.91	45.9 ± 8.54
	Patch-based TDA ($6 \times 6 \times 6$, [iqr, entropy])	LR	75.16 ± 8.97	73.05 ± 9.25	60 ± 20	81.15 ± 10.57	57.22 ± 14.94
CRLM	Cubical Complex	LR	52.88 ± 2.79	54.14 ± 4.39	55.99 ± 10.35	50.85 ± 6.19	48.44 ± 5.37
	Patch-based TDA ($5 \times 5 \times 5$, [median, entropy, max])	LR	60 ± 2.11	63.1 ± 2.71	58.92 ± 7.29	60.74 ± 5.73	53.96 ± 3.33
Average Improvement			10.38	6.94	2.06	11.58	8.51

Table 4: The Results of Benchmarking the Patch-Based TDA Against the Cubical Complex Approach in Terms of the Required Time To Compute PH in Dimensions Zero, One and Two Across All Datasets

Dataset	Image Size	Method	Patch size	Stats	Points Dimension	Time (s)
KiTS19	$57 \times 220 \times 220$	Patch-Based	$6 \times 6 \times 6$	mean, median, range	4D	0.26
		Cubical Complex	-	-	-	33.40
FLARE22	$102 \times 290 \times 330$	Patch-Based	$4 \times 4 \times 4$	mode, entropy	3D	2.54
		Cubical Complex	-	-	-	124.03
Pancreas Tumours	$33 \times 120 \times 120$	Patch-Based	$6 \times 6 \times 6$	iqr, entropy	3D	0.07
		Cubical Complex	-	-	-	5.14
CRLM	$87 \times 323 \times 400$	Patch-Based	$5 \times 5 \times 5$	median, entropy, max	4D	31.69
		Cubical Complex	-	-	-	139.52

4 Python Package

Code reusability is a crucial aspect in the computational implementation of a newly developed algorithm. Therefore, we provide a convenient python package, called Patch-TDA, to facilitate experimentation with the proposed approach. The package can be downloaded directly from the corresponding GitHub repository. ¹

5 Conclusion

This work introduced a novel patch-based PH construction method for 3D CT imaging data, a significant improvement over the cubical complex filtration, the traditional approach of building PH from grid-structured data and to overcome the computational burden of the later method, in particular, with high resolution volumetric data. The process of transforming a 3D image patch to a point, a crucial component of the proposed method, was systematically analyzed and numerous experiments were conducted in this regard. Four datasets of 3D CT images were considered to comprehensively assess the proposed approach. Our result suggests that utilizing stats as a patch-to-point transformation method, which eventually convert all patches of a 3D volume to a point cloud upon which PH can be constructed, yields better results in downstream analysis than using PCA. Furthermore, we benchmarked our method in terms of classification performance and also time-efficiency against the cubical complex filtration. It was concluded that the proposed technique for building PH from 3D CT images outperformed the later one in both benchmarking tests. A limitation of this work could be the lack of inclusion of further medical imaging datasets and modalities. There are several possible future research directions to further improve the performance of the patch-based TDA method, such as reducing the number of points in the point cloud via clustering methods. In addition, the method could also be deployed as a feature extraction mechanism, for instance in an LSTM neural network to take advantage of the robustness of the method in capturing temporal information.

Acknowledgments

This work was funded by National Institutes of Health grants R01CA233888 and SP0RE grant P50CA257881.

References

- [1] Marius E Mayerhoefer, Andrzej Materka, Georg Langs, Ida Häggström, Piotr Szczypiński, Peter Gibbs, and Gary Cook. Introduction to radiomics. *Journal of Nuclear Medicine*, 61(4):488–495, 2020.
- [2] Joonsang Lee, Angela Steinmann, Yao Ding, Hannah Lee, Constance Owens, Jihong Wang, Jinzhong Yang, David Followill, Rachel Ger, Dennis MacKin, et al. Radiomics feature robustness as measured using an mri phantom. *Scientific reports*, 11(1):3973, 2021.

¹<https://github.com/dashtiali/patch-tda>

- [3] Stefania Rizzo, Francesca Botta, Sara Raimondi, Daniela Origgi, Cristiana Fanciullo, Alessio Giuseppe Morganti, and Massimo Bellomi. Radiomics: the facts and the challenges of image analysis. *European radiology experimental*, 2:1–8, 2018.
- [4] Yoichi Hayashi. The right direction needed to develop white-box deep learning in radiology, pathology, and ophthalmology: A short review. *Frontiers in Robotics and AI*, 6:24, 2019.
- [5] Alanna Vial, David Stirling, Matthew Field, Montserrat Ros, Christian Ritz, Martin Carolan, Lois Holloway, and Alexis A Miller. The role of deep learning and radiomic feature extraction in cancer-specific predictive modelling: a review. *Translational Cancer Research*, 7(3), 2018.
- [6] Taban Majeed, Rasber Rashid, Dashti Ali, and Aras Asaad. Issues associated with deploying cnn transfer learning to detect covid-19 from chest x-rays. *Physical and Engineering Sciences in Medicine*, 43(4):1289–1303, 2020.
- [7] Gunnar Carlsson. Topology and data. *Bulletin of the American Mathematical Society*, 46(2):255–308, 2009.
- [8] Pek Y Lum, Gurjeet Singh, Alan Lehman, Tigran Ishkanov, Mikael Vejdemo-Johansson, Muthu Alagappan, John Carlsson, and Gunnar Carlsson. Extracting insights from the shape of complex data using topology. *Scientific reports*, 3(1):1236, 2013.
- [9] Eashwar Somasundaram, Adam Litzler, Raoul Wadhwa, Rowan Barker-Clarke, and Jacob Scott. Persistent homology of tumor ct scans is associated with survival in lung cancer. *Medical physics*, 48(11):7043–7051, 2021.
- [10] Naoya Tanabe, Shizuo Kaji, Susumu Sato, Tomoo Yokoyama, Tsuyoshi Oguma, Kiminobu Tanizawa, Tomohiro Handa, Takashi Sakajo, and Toyohiro Hirai. A homological approach to a mathematical definition of pulmonary fibrosis and emphysema on computed tomography. *Journal of Applied Physiology*, 131(2):601–612, 2021.
- [11] Dashti A Ali, Jacob J Peoples, Richard KG Do, William R Jarnagin, Aras T Asaad, and Amber L Simpson. A pca-based tda approach for computed tomography. In *Proceedings of SPIE Medical Imaging 2026: Computer-Aided Diagnosis*, Vancouver, BC, Canada, 2026. to appear.
- [12] Yashbir Singh, Colleen M Farrelly, Quincy A Hathaway, Tim Leiner, Jaidip Jagtap, Gunnar E Carlsson, and Bradley J Erickson. Topological data analysis in medical imaging: current state of the art. *Insights into Imaging*, 14(1):58, 2023.
- [13] Yoshiki Kawata, Noboru Niki, Masahiko Kusumoto, Hironobu Ohamatsu, Keiju Aokage, Genichiro Ishii, Yuji Matsumoto, Takaaki Tsuchida, Kenji Eguchif, and Masahiro Kaneko. Representation of texture structures with topological data analysis for stage ia lung adenocarcinoma in three-dimensional thoracic ct images. In *Medical Imaging 2021: Biomedical Applications in Molecular, Structural, and Functional Imaging*, volume 11600, pages 106–112. SPIE, 2021.
- [14] Valentina Podoia, Jenny Haefeli, Kazuhito Morioka, Hsiang-Ling Teng, Lorenzo Nardo, Richard B Souza, Adam R Ferguson, and Sharmila Majumdar. Mri and biomechanics multidimensional data analysis reveals $r2-r1\rho$ as an early predictor of cartilage lesion progression in knee osteoarthritis. *Journal of Magnetic Resonance Imaging*, 47(1):78–90, 2018.
- [15] Francisco Belchi, Mariam Pirashvili, Joy Conway, Michael Bennett, Ratko Djukanovic, and Jacek Brodzki. Lung topology characteristics in patients with chronic obstructive pulmonary disease. *Scientific reports*, 8(1):5341, 2018.
- [16] Asuka Oyama, Yasuaki Hiraoka, Ipepe Obayashi, Yusuke Saikawa, Shigeru Furui, Kenshiro Shiraishi, Shinobu Kumagai, Tatsuya Hayashi, and Jun’ichi Kotoku. Hepatic tumor classification using texture and topology analysis of non-contrast-enhanced three-dimensional t1-weighted mr images with a radiomics approach. *Scientific reports*, 9(1):8764, 2019.
- [17] Robin Vandaele, Pritam Mukherjee, Heather Marie Selby, Rajesh Pravin Shah, and Olivier Gevaert. Topological data analysis of thoracic radiographic images shows improved radiomics-based lung tumor histology prediction. *Patterns*, 4(1), 2023.
- [18] Manish Saggarr, Olaf Sporns, Javier Gonzalez-Castillo, Peter A Bandettini, Gunnar Carlsson, Gary Glover, and Allan L Reiss. Towards a new approach to reveal dynamical organization of the brain using topological data analysis. *Nature communications*, 9(1):1399, 2018.
- [19] Bryon R Gomberg, Punam K Saha, Hee Kwon Song, Scott N Hwang, and Felix W Wehrli. Topological analysis of trabecular bone mr images. *IEEE transactions on medical imaging*, 19(3):166–174, 2000.
- [20] Nina Otter, Mason A Porter, Ulrike Tillmann, Peter Grindrod, and Heather A Harrington. A roadmap for the computation of persistent homology. *EPJ Data Science*, 6:1–38, 2017.
- [21] Vidit Nanda and Radmila Sazdanović. Simplicial models and topological inference in biological systems. In *Discrete and topological models in molecular biology*, pages 109–141. Springer, 2013.

- [22] Gunnar Carlsson. Topological pattern recognition for point cloud data. *Acta Numerica*, 23:289–368, 2014.
- [23] Raoul Bott and Loring W Tu. *Differential forms in algebraic topology*, volume 82. Springer Science & Business Media, 2013.
- [24] Chi Seng Pun, Si Xian Lee, and Kelin Xia. Persistent-homology-based machine learning: a survey and a comparative study. *Artificial Intelligence Review*, 55(7):5169–5213, 2022.
- [25] Adélie Garin and Guillaume Tauzin. A topological" reading" lesson: Classification of mnist using tda. In *2019 18th IEEE International Conference On Machine Learning And Applications (ICMLA)*, pages 1551–1556. IEEE, 2019.
- [26] Christoph D Hofer, Roland Kwitt, and Marc Niethammer. Learning representations of persistence barcodes. *Journal of Machine Learning Research*, 20(126):1–45, 2019.
- [27] Yu-Min Chung and Austin Lawson. Persistence curves: A canonical framework for summarizing persistence diagrams. *Advances in Computational Mathematics*, 48(1):6, 2022.
- [28] Ilya Chevyrev, Vidit Nanda, and Harald Oberhauser. Persistence paths and signature features in topological data analysis. *IEEE transactions on pattern analysis and machine intelligence*, 42(1):192–202, 2018.
- [29] Eric Berry, Yen-Chi Chen, Jessi Cisewski-Kehe, and Brittany Terese Fasy. Functional summaries of persistence diagrams. *Journal of Applied and Computational Topology*, 4(2):211–262, 2020.
- [30] Harish Chintakunta, Thanos Gentimis, Rocio Gonzalez-Diaz, Maria-Jose Jimenez, and Hamid Krim. An entropy-based persistence barcode. *Pattern Recognition*, 48(2):391–401, 2015.
- [31] Dashti Ali, Aras Asaad, Maria-Jose Jimenez, Vidit Nanda, Eduardo Paluzo-Hidalgo, and Manuel Soriano-Trigueros. A survey of vectorization methods in topological data analysis. *IEEE Transactions on Pattern Analysis and Machine Intelligence*, 2023.
- [32] Guy M Morton. *A computer oriented geodetic data base and a new technique in file sequencing*. International Business Machines Company, 1966.
- [33] Herbert Edelsbrunner, David Kirkpatrick, and Raimund Seidel. On the shape of a set of points in the plane. *IEEE Transactions on information theory*, 29(4):551–559, 1983.
- [34] Jean-Daniel Boissonnat, Frédéric Chazal, and Mariette Yvinec. *Geometric and topological inference*, volume 57. Cambridge University Press, 2018.
- [35] Nicholas Heller, Niranjana Sathianathan, Arveen Kalapara, Edward Walczak, Keenan Moore, Heather Kaluzniak, Joel Rosenberg, Paul Blake, Zachary Rengel, Makinna Oestreich, et al. The kits19 challenge data: 300 kidney tumor cases with clinical context, ct semantic segmentations, and surgical outcomes. *arXiv preprint arXiv:1904.00445*, 2019.
- [36] MA. MICCAI FLARE22 challenge dataset (50 labeled abdomen CT scans), 2023.
- [37] Jun Ma, Yao Zhang, Song Gu, Cheng Zhu, Cheng Ge, Yichi Zhang, Xingle An, Congcong Wang, Qiyuan Wang, Xin Liu, et al. Abdomenct-1k: Is abdominal organ segmentation a solved problem? *IEEE Transactions on Pattern Analysis and Machine Intelligence*, 44(10):6695–6714, 2021.
- [38] Mohammad Hamghalam, Richard KG Do, and Amber L Simpson. Attention-based ct scan interpolation for lesion segmentation of colorectal liver metastases. In *Medical Imaging 2023: Biomedical Applications in Molecular, Structural, and Functional Imaging*, volume 12468, pages 186–193. SPIE, 2023.
- [39] Katharina S Winter, Felix O Hofmann, Kolja M Thierfelder, Julian W Holch, Nina Hesse, Alena B Baumann, Dominik P Modest, Sebastian Stintzing, Volker Heinemann, Jens Ricke, et al. Towards volumetric thresholds in recist 1.1: Therapeutic response assessment in hepatic metastases. *European Radiology*, 28:4839–4848, 2018.